



# PERFORMANCE CHARACTERISTICS OF HUMPBACK WHALE TUBERCLES AT LOW REYNOLDS NUMBERS

H. Ladha<sup>1</sup>, M. A. Gandhi<sup>2</sup>, K. Singh<sup>3</sup> and S. M. Dakka<sup>4\*</sup>

Faculty of Engineering, University of Nottingham, Nottingham NG7 2RD, UK, <sup>1</sup>Email: [hladha125@gmail.com](mailto:hladha125@gmail.com),

<sup>2</sup>Email: [u19me041@med.svnit.ac.in](mailto:u19me041@med.svnit.ac.in), <sup>3</sup>Email: [Kuldeep.Singh@nottingham.ac.uk](mailto:Kuldeep.Singh@nottingham.ac.uk), <sup>4</sup>Email: [Sam.Dakka@nottingham.ac.uk](mailto:Sam.Dakka@nottingham.ac.uk)

## Abstract:

Many marine vessels and small unmanned air vehicles operate at low  $Re$  flow regimes. Due to their small size and low operational velocities, they face increased stall severity, which is a crucial challenge to overcome. Tubercle Leading Edge (TLE) aerofoils can be exploited to solve this issue. Akin to passive flow control devices, tubercles generate counter-rotating vortex pairs on aerofoils, with vorticity being proportional to amplitude to wavelength ratio thus augmenting lift, and delaying flow separation. Performance improvements such as reduced drag, reduced stall severity, and improved post-stall characteristics are achieved using TLE designs. This investigation experimentally and numerically is focused on the performance characteristics of three designed TLE aerofoils at a relatively low  $Re$  value of  $1 \times 10^5$ . Limited studies are available on this low  $Re$  flow regime, hence the novelty of this investigation. The aims were to build upon the literature and to determine the best TLE aerofoil variant for further investigation, development, and eventual system-level implementation in a small naval or air vehicle design. The TLE aerofoil models investigated, 'A4 $\lambda$ 25', 'A8 $\lambda$ 25', and 'A12 $\lambda$ 25' which specify the tubercle amplitude and wavelength in mm delivered weaker and delayed stall, reduced pre-stall drag, and improved post-stall lift. The 'A4 $\lambda$ 25' model offered the best combination of increased pre-stall lift, reduced pre-stall drag, and post-stall lift. Further investigation on the 'A4 $\lambda$ 25' variant's performance within the context of an engineered system is worthwhile for realizing its application in low  $Re$  flight.

**Keywords:** Humpback whale tubercles, computational fluid dynamics, low Reynolds flows, vortex generators.

## NOMENCLATURE

$A$	Amplitude, m	$C_D$	Drag Coefficient
$c$	Chord, m	$SD$	standard deviation
$h$	Height, m	$n$	number of values across experiments
$s$	Span, m	$x_i$	data value
$V$	Velocity, m/s	$\bar{x}$	mean of data values
$Re$	Reynolds number	$SE$	standard error
$S$	Wing Area, m <sup>2</sup>	$C_p$	Pressure Coefficient
$h$	Manometer height, mm	$a$	Ambient
$g$	Gravity, m/s <sup>2</sup>	w	Wind tunnel
$P$	Air Pressure, Pa	<b>Greek symbols</b>	
$T$	Temperature, K	$\alpha$	angle of attack
$L$	Lift Force, N	$\lambda$	Wavelength, m
$D$	Drag Force, N	$\delta$	Boundary layer thickness, mm
$C_L$	Lift Coefficient	$\rho$	Density, kg/m <sup>3</sup>

## 1. Introduction

In aerodynamics and marine technology, lift and drag are fundamental. Aerodynamicists and marine scientists continually seek to maximize aerodynamic efficiency. Persistent progress and innovation in aeronautics and

naval architectures results in an incremental efficiency and safety improvements. Regardless of a system's scale and importance, benefits can be realized throughout the industry when novel technology is utilized. Some novel aerospace innovations have been bio-inspired and have provided great benefits. Biomimicry is nature-inspired design. Studying how animals are adapted to their environment can enable engineering innovation. 'Sharklets' to reduce induced drag, V-formation flight to reduce fuel consumption, and morphing wing technology to provide improved aerodynamic adaptability are all examples of biomimetic design (Airbus, 2021). Therefore, biomimicry is a useful tool for overcoming engineering challenges. Another biomimetic technology is the tubercle leading edge (TLE) for aircraft wings. Inspired by humpback whales (Fig. 1), this technology delivers improved lift and drag characteristics and is already successfully utilized in wind turbines and fans (turbines and fans inspired by whales, 2018) for its improved efficiency. However, TLE technology is not commonplace in aerospace and marine technology design since it requires further study and optimization. Many experimental and numerical studies have investigated TLE wing performance in Re ranges typically greater than 100,000. A relevant application of TLE wings is within micro aerial vehicles (MAV) and small unmanned aerial vehicle (UAV) designs in addition to control fins in vessels and submarines (Bal, 2024, Ray et al, 2016, Sakthivel et al., 2011). The flight velocities of small aerial vehicles are drastically lower than conventional aircraft, resulting in significantly lower Re flight regimes. The key issue surrounding low Re flight is reduced stability due to the increased stall severity. TLE wings provide performance gains such as reduced drag, reduced stall severity, improved aerodynamic efficiency, and improved post-stall flight characteristics. Therefore, small aerial vehicles, which are abundantly utilized nowadays, can benefit from TLE wing designs.

In this investigation, the performance of three NACA0012 TLE aerofoils designs were investigated. The aims were to build upon the literature of low Re performance of TLE wings and to determine the most suitable design for low Re flight regimes. The TLE wing variants were designed using CAD and manufactured via 3D printing. After post-processing the manufactured aerofoil models, experimental analysis was conducted using wind tunnel testing. The aerodynamic forces were measured, and the flow mechanics were studied using oil flow visualization.



Fig. 1 : The nodules on the leading edge of the humpback whale's pectoral flipper aids its hydrodynamic manoeuvrability (WDC, 2012).

### 1.1 Discovery of the tubercle effect

The hydrodynamic agility of humpback whales is attributed to their tubercle-lined flippers, which enable tighter banking within the water by providing increased lift. This aids their feeding behavior, where they trap their prey by encircling them in a shroud of bubbles and subsequently lunge inwards to capture their prey (Watts and Fish, 2001), (Bandyopadhyay, 2009). Marine biologist F. Fish and aeronautical engineer P. Watts initially

investigated the tubercles' purpose. A scale model of the humpback whale flipper was tested, and the leading-edge tubercles were indeed discovered to be advantageous, as they simultaneously aided lift, reduced drag, and reduced stall severity. An increased  $C_L$  and reduced  $C_D$  was observed compared to the baseline (without tubercles) model (Dewar et al., 2018). Following this, Fish and Watts patented the TLE technology, founding Whale Power and pioneering industrial ceiling fans and wind turbine blades with TLEs. These designs were highly successful, providing 25% more airflow and 20% more energy than conventional wind turbine blades (Aftab et al., 2016).

## 1.2 Past research

Since Fish and Watts' initial research, numerous studies investigated TLE wings. Certain studies are more noteworthy due to their comparable  $Re$  values. An investigation of  $Re$  value is crucial, as consistent comparisons can only be made between studies in similar  $Re$  ranges.  $Re$  is the ratio between inertial and viscous forces as expressed by Eqn. (1). It dictates the regime that moving bodies experience. It's a function of the body's characteristic length, ' $L$ ', fluid flow velocity, ' $V$ ', and fluid properties ' $\rho$ ' and ' $\mu$ '.

$$Re = \frac{\rho VL}{\mu} \quad (1)$$

Alternative TLE studies have also utilized a NACA 0021 aerofoil. Hansen used hydrogen bubble visualization to assess three TLE configurations at a  $Re$  of 120,000 (Hansen et al., 2011, Hansen, 2012). The TLE profiles investigated were ' $A2\lambda7.5$ ', ' $A4\lambda15$ ', and ' $A8\lambda30$ '. The abbreviated names specify the tubercle amplitude and wavelength in mm. Improved stall delay and  $C_{L,max}$  were achieved in the smallest amplitude variant. Flow visualization demonstrated that stall prematurely occurred in the trough and that the tubercles functioned like vortex generators.

Another NACA 0021 TLE wing was computationally studied by (Skillen et al., 2014) at a  $Re$  of 120,000. The TLE wing employed a 15% $c$  and 21% $c$  amplitude and wavelength respectively. A 36% increase in lift and 25% decrease in drag was achieved versus the baseline model (Gopinathan and Ralphin, 2022).

(Rostamzadeh et al., 2013, 2014) investigated large  $A/\lambda$  ratio TLE wings at a  $Re$  of 120,000. Post-stall performance improvements were observed in the TLE variant. Tubercles were deemed to be detrimental to pre-stall flight, yet beneficial in post-stall flight due to the secondary vortices which enhanced momentum transfer in the flow at  $\alpha = 15^\circ$ . These secondary vortices occupied a large delta-shaped region in the trailing edge vicinity. Other observations included vorticity being proportional to  $A/\lambda$ . Despite increased vorticity in larger  $A/\lambda$  ratio TLEs, poorer pre-stall lift generation was observed in these studies. Additional computational analysis depicted the formation mechanism of the streamwise vortices. Described by '*Prandtl's secondary flow of the first-kind*' (a skew-induced turbulent driven flow), this mechanism arises from the (streamwise) curvature variation along the TLEs peak and trough. The resulting transverse pressure gradient along the TLE induces vorticity (Pattison, 2011). Importantly, Rostamzadeh's study significantly contributed to the understanding of TLE flow mechanics.

Regarding TLE optimization for wings using the NACA 0021 aerofoil, these studies suggest that a smaller tubercle amplitude is more beneficial overall.

## 1.3 Flow physics

The past research suggests that tubercles function as passive flow control devices, generating pairs of counter-rotating streamwise vortices (shown in Figure 2) akin to vortex generators (Aftab et al., 2016, Gopinathan and Ralphin, 2022).

Leading-edge tubercles are like a series of delta wings with a curved apex over the wingspan. They generate streamwise vortices on the aerofoil suction (upper) surface. The boundary layer is re-energised from the downwash imposed by the vortices at the tubercle peaks. Despite the adverse pressure gradient, this achieves delayed flow separation upon the aerofoil upper surface. Therefore, compared to their baseline counterparts, TLE wings exhibit softer stall at higher angles of attack by resisting the growth of the laminar separation bubble. At the tubercle troughs, the vortices impose an upwash, limiting flow separation to the immediate vicinity and

providing increased lift at high angles of attack. Overall, the vortices impede flow separation and reduce the drag penalty.

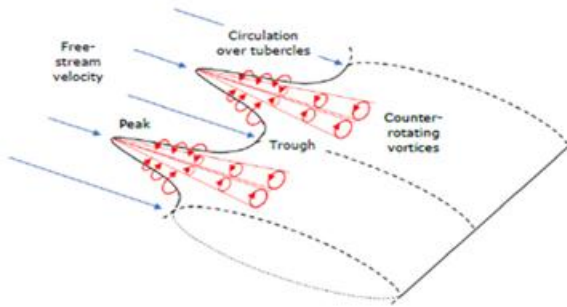


Fig. 2(a): Simplified 3D

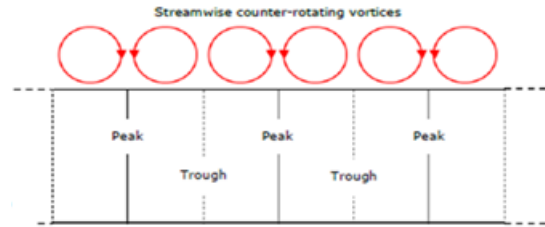


Fig. 2(b): Head on diagram of flow mechanics over a TLE wing section.

## 2. Methodology

### 2.1 Experimental setup and procedure

Shown in Figure 2, The TecQuipment AF100 wind tunnel was used in this investigation. Its working section has the dimensions 305mm × 305mm × 600mm. Models were held in the test section with a mounting rod and their angle of attack ( $\alpha$ ) was externally controlled, using the dial on the ‘Three Component Balance Instrumentation’ fixed to the screen side. The wind tunnel speed was controlled by adjusting the manometer fluid height on the ‘Control and Instrumentation Frame’ (mounted onto the ‘Main Frame’).

The manometer height corresponds to the wind tunnel velocity. Based on  $Re$  of 100,000, the required wind tunnel velocity was determined to be 18.6m/s from (1) and the manometer fluid height was calculated as 21.8mm from Eqn. (2).

$$h = \frac{0.5 \frac{P_a}{RT_a} V^2}{\rho_w g} \quad (2)$$

A laptop was connected to the ‘VDAS-F Hardware’ on the ‘Control and Instrumentation Frame’ via a USB connection. Lift and drag data were recorded using the ‘Timed Data Capture’ function within the ‘VDAS Software’, which enabled data sampling at a specified frequency. To ensure maximum fidelity, 40 readings were sampled using a  $\Delta t = 0.5s$  for each angle of attack. Subsequently, data was exported, and post-processing was conducted, which involved averaging the lift and drag data for each angle of attack and non-dimensionalization of the data, as outlined in (3) and (4). In the equations, ‘L’ and ‘D’ are lift and drag respectively, ‘ $\rho$ ’ is the air density, ‘V’ is the air velocity, and ‘S’ is the wing area. Experiments were repeated at least three times for each model.

$$C_L = \frac{2L}{\rho V^2 S} \quad (3)$$

$$C_D = \frac{2D}{\rho V^2 S} \quad (4)$$

Considerations of minimizing wind tunnel blockage and wall interference effects were made. Blockage ratios within 5-10% are deemed acceptable. Wall interference effects occur when the model is too close to the test section walls and disrupts the boundary layer. The boundary layer thickness, ‘ $\delta$ ’, in the test section walls was determined to be 22.2mm from (5). Wall interference was not an issue since there was adequate distance on either side of the wing models in the test section.

$$\delta = \frac{0.37x}{Re^{\frac{1}{5}}} \quad (5)$$

Flow visualization studies were also conducted. An oil mixture consisting of titanium dioxide ( $TiO_2$ ), linseed oil, and paraffin oil in a 1:1:10 wt.% ratio respectively was used. Visualization was conducted at a speed of 18.6m/s (to achieve  $Re = 100,000$ ). In the test section, the oil mixture was painted over the aerofoil upper surface. The wind tunnel was turned on and the flow development was recorded using a camera. Images were simultaneously captured during and after establishment of the fully developed flow. This procedure was

repeated for  $\alpha$  values of  $0^\circ$ ,  $5^\circ$ ,  $10^\circ$  across all three TLE wing models. Information on oil flow visualization procedure and camera specifications are available on appendix section.

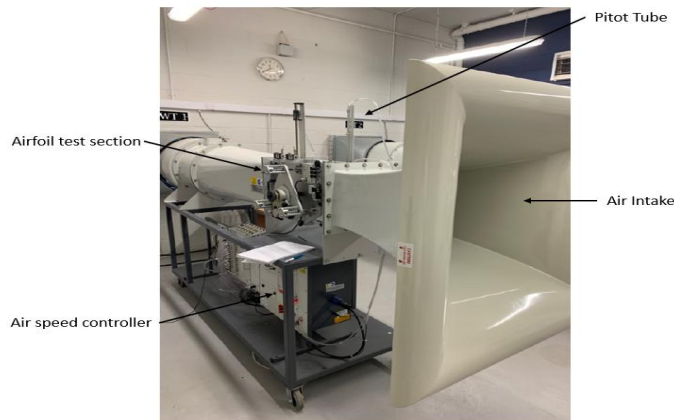


Fig. 3: AF100 subsonic wind tunnel (TecQuipment Ltd, 2010)

### 2.1.1 Wing design and manufacture

Several constraints governed wing sizing. These were the test section dimensions, sizing for minimizing blockage and wall-effects to be inconsequential, and sizing for manufacturing capability via the available 3D printers. The investigation of  $Re$  of 100,000 also dictated the aerofoil chord length, ' $c$ ', which is represented by the characteristic length, ' $L$ ', in (1). The resulting designs had a 250mm wingspan and 80mm chord length. Three TLE aerofoils were derived from a 'Baseline' aerofoil. Past research suggests that tubercle wavelength variation only modestly impacts TLE aerofoil performance, whereas amplitude variation provides more prominent performance improvements (Aftab et al., 2016). Therefore, only tubercle amplitude was varied in this investigation. For the three TLE aerofoils designed, 'A4 $\lambda$ 25', 'A8 $\lambda$ 25', and 'A12 $\lambda$ 25', the values correspond to the amplitude and wavelength in mm. Since larger tubercles generate increased vorticity, an amplitude range of  $5\%c - 15\%c$  was chosen. The tubercle sizing in this investigation is unique from previous investigations which have focused on smaller tubercles in amplitude  $A \leq 12\%c$  range. The wavelength,  $\lambda = 31.25\%c$  (25mm/80mm) was chosen as it corresponds to the average tubercle wavelength utilized in past research (Aftab et al., 2016), (Gopinathan and Ralphin, 2022). 'CATIA' was used to design the TLE aerofoils. From Airfoil Tools (n.d.), NACA 0021 aerofoil coordinates were obtained and plotted the aerofoil points directly in the 'Generative Wireframe and Surface' app. After modelling, the geometry was solidified in the 'Part Design' app.

3D printing using a polylactic acid (PLA) filament was utilized for manufacturing. Model refinement was required to achieve a high-quality surface finish. This procedure involved sanding, applying filler, further sanding, priming, and applying a topcoat layer of gloss black acrylic. The resulting wing models had a smooth surface finish suitable for experimental activities as seen in Figure 4



Fig. 4: Designed wings – 'A12 $\lambda$ 25', 'A8 $\lambda$ 25', 'A4 $\lambda$ 25', and 'Baseline' from left to right.

The TLE aerofoils were designed such that the tubercle troughs receded from the leading edge. With all the having a chord length of 80mm (tubercle peak to trailing edge in the TLE variants), each aerofoil area was unique, and an increasing tubercle amplitude resulted in diminishing wing area. The ‘Baseline’ model had an area of 0.02m<sup>2</sup>. The leading edge of the TLE wings follow a sinusoidal shape. Numerical integration was used to calculate the TLE aerofoils areas  $f(x)=0.5[A+A\cos(x)]$  was plotted from 0 to  $2\pi$  (where A is the tubercle amplitude for the respective TLE aerofoil). The midpoint rule with  $\Delta x = 0.001$  was used to evaluate the integral. The resulting area was multiplied by the total number of tubercles (ten) and added to the rectangular region’s area beneath. The wing areas for ‘A4λ25’, ‘A8λ25’, and ‘A12λ25’ were 0.01913m<sup>2</sup>, 0.01825m<sup>2</sup>, and 0.01738m<sup>2</sup> respectively.

## 2.2 Computational model

According to the experimental findings, TLE model "A4λ25" is the most effective TLE of the three. As a result, the model was chosen for additional computational study. In order to better understand the flow mechanism, this investigation includes creating a computational domain and mesh for the TLE model for various angles of attack as well as examining their aerodynamic properties and flow visualization

### 2.2.1 Computational domain

The computational domain considered in the present study mimics the experimental test section as shown in Figure 5.

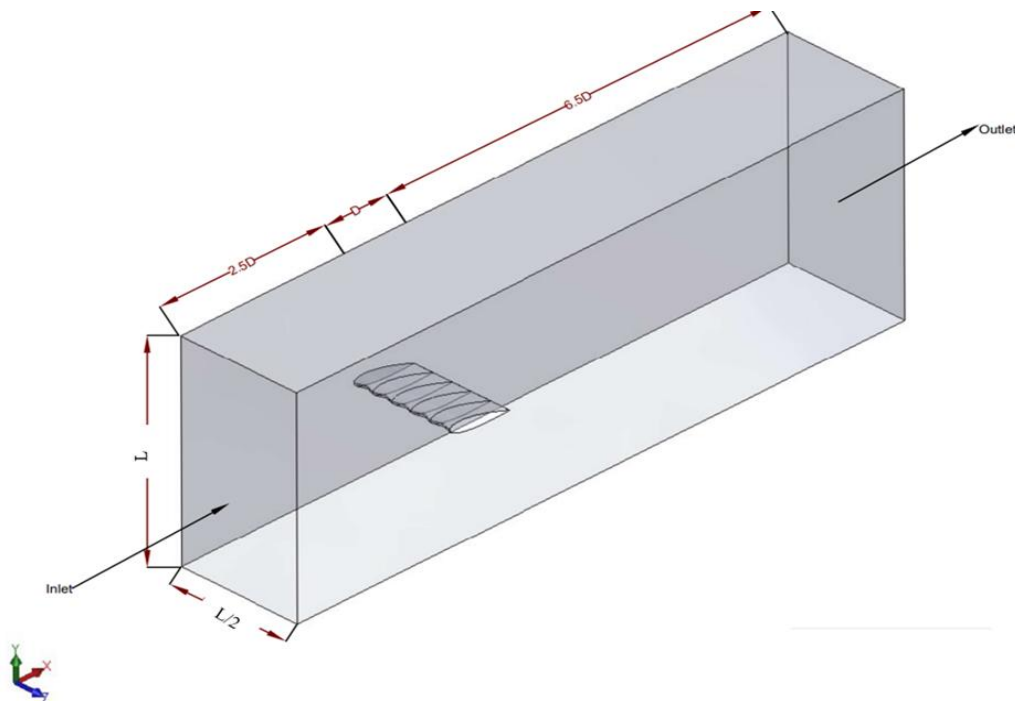


Fig. 5: Computational Domain for A4λ25 at AOA 10°.

The size of the computational domain is 800mm×305mm×152.5mm. The inlet was 220 mm upstream of the leading edge of the wing. The wingspan of the half wing is 125mm. D is the length of the chord which is 80mm and the width of the domain L is 305 mm.

### 2.2.2 Mesh and boundary condition

In the present study, polyhedral cells are used to discretize the computational domain. An inflation layer is added in the normal direction to the surface of the wing. The first cell centre of the inflation layer is kept at 7.5 μm from the surface of the wing with an overall cell count of 5.5 million. A typical mesh is shown in Figure 6 for the model at AOA 25°.

The boundary conditions imposed on the computational domain are indicated in Figure 6. All components of velocity level are provided at the inlet calculated based on the Reynolds number. The pressure outlet boundary condition is specified at the outlet of the domain with zero-gauge pressure. Half of the experimental tunnel is modelled in the width direction and a symmetry boundary condition is imposed on the face. All other surfaces are treated as non-slip walls.

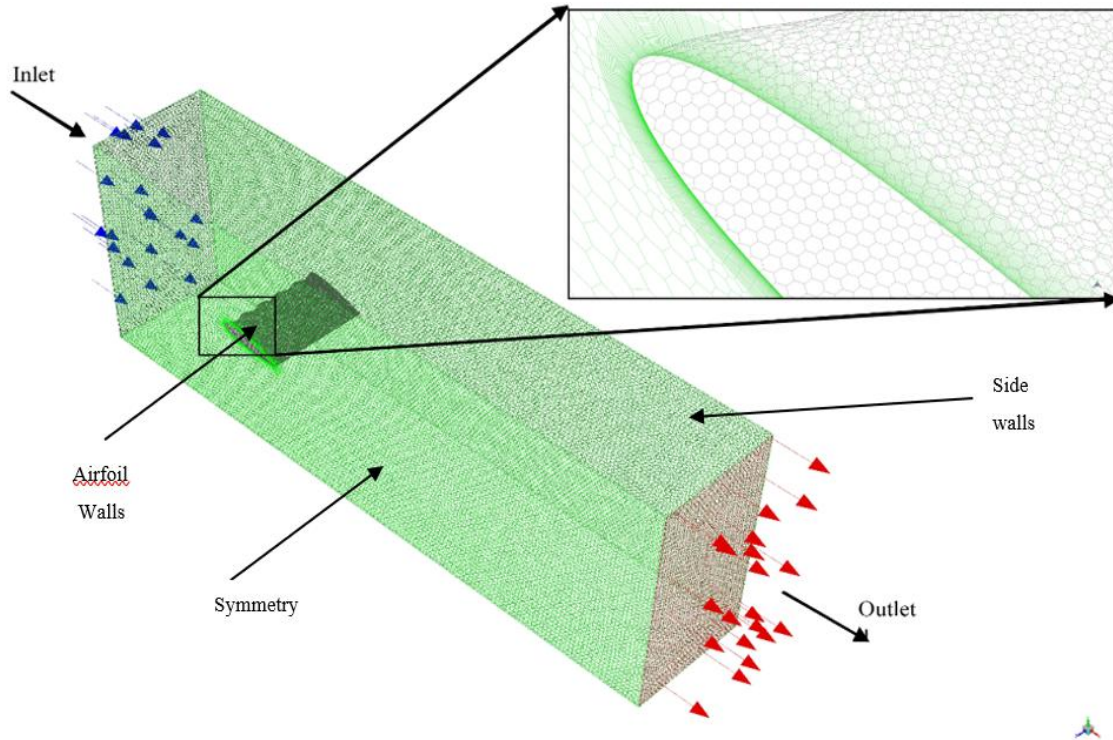


Fig. 6: A typical mesh at AOA 25° used in the present study.

### 2.2.3 Solution procedure

The time-averaged continuity and momentum equations (Eq. 6 and Eq. 7) are solved using a commercial CFD solver ANSYS Fluent (ANSYS, 2018) which is based on the finite volume method. Air at ambient pressure is considered as a working fluid.

$$\frac{\partial \bar{u}_i}{\partial x_i} = 0 \quad (6)$$

$$\rho \bar{u}_j \frac{\partial \bar{u}_i}{\partial x_j} = -\frac{\partial \bar{p}}{\partial x_i} + \frac{\partial}{\partial x_j} \left[ \mu \left( \frac{\partial \bar{u}_i}{\partial x_j} + \frac{\partial \bar{u}_j}{\partial x_i} - \overline{\rho u_i' u_j'} \right) \right] \quad (7)$$

The second-order upwind interpolation scheme is used to discretize all governing equations. For pressure-velocity coupling, SIMPLE algorithm proposed by Patankar (Patankar, 1980) is utilized. In this study, the two-equation RANS model SST k-omega is used following (Lositaño and Danao, 2019) for turbulence modelling. The convergence criterion for the governing equations was to  $10^{-5}$  for residual level.

### 2.2.3 Grid sensitivity analysis

In the present study, a grid sensitivity analysis is carried out to optimize the grids required. The grid resolution is systematically increased such that the refined grid has 1.5 times the cells count or previous mesh following the recommendation of (Celik, 2005). Three grids having a number of cells 926,920 (Mesh-1), 1,824,345 (Mesh-2) and 2,795,945 (Mesh-3) were investigated for the test case at AOA= 20°. Pressure coefficient ( $C_p$ ) on the aerofoil at a location  $Z/\lambda = 0.2$  and wake velocity at  $X/D = 2$  downstream of leading edge of wing is selected to access the grid sensitivity. The pressure coefficient and non-dimensional axial velocity are presented in Figure 7 to demonstrate grid independence of the solution. It can be observed from figure 7 (a) that pressure coefficient distribution deviates for Mesh-1 as compared to Mesh-2 and Mesh-3 in the range of  $-0.15 < X/D < 0.15$ ,

elsewhere numerical predictions are comparable. The averaged deviation in the predictions of pressure coefficient by Mesh-2 and Mesh-3 is less than 0.5%.

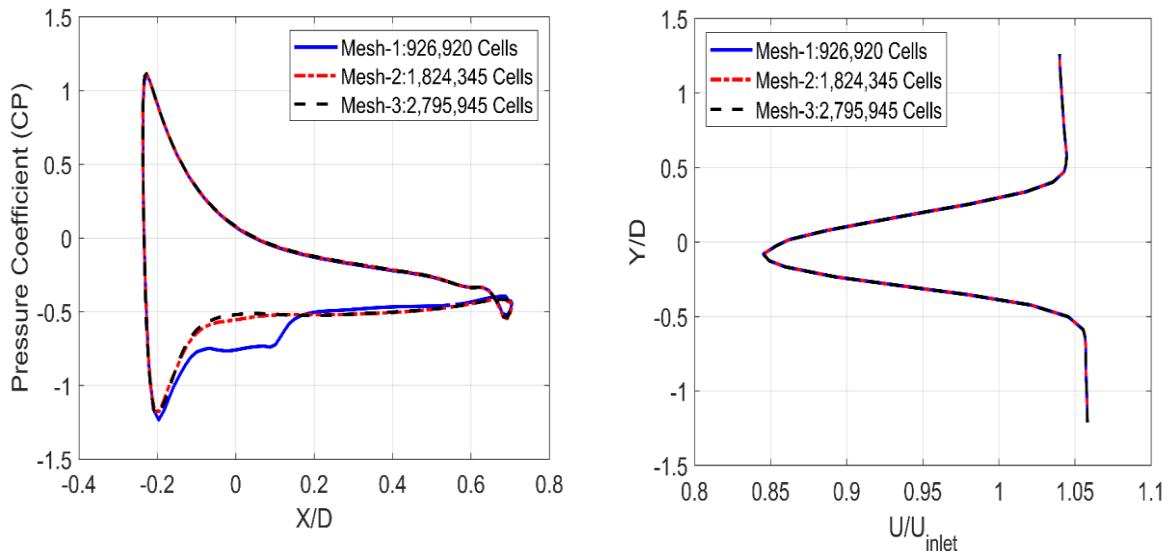


Fig. 2(a): Variation of pressure coefficient at  $Z/\lambda = 0.2$  Fig. 7(b): Non-dimensional wake velocity at  $X/D = 2$  downstream of the leading edge.

The wake velocity has a significant impact on the drag and lift coefficient and hence it was decided to consider it as a parameter to determine grid independence of the solution. The non-dimensional velocity in the wake region at a downstream distance  $X/D = 2$  from the leading edge of the wing is shown in Figure 7(b). It can be observed that the wake velocity predicted by all the grids is identical. The average difference in the prediction of wake velocity was less than 0.25%. Additionally, lift and drag coefficient is recorded for these grids for the tested case i.e.,  $AOA = 20^\circ$  as given in Table -1. The deviation in the drag coefficient is 1.57% for Mesh-2 and Mesh-1 and 0.4% for Mesh-3 and Mesh-2. Likewise, the deviation in the lift coefficient is 2.83% for Mesh-2 and Mesh-1 and 0.21% for Mesh-3 and Mesh-2. The numerical predictions of Mesh-2 and Mesh-3 are comparable and hence Mesh-2 is selected for further studies to minimize the computational cost.

Table- 1: Drag and Lift coefficient obtained from the investigated grids for  $AOA = 20^\circ$ .

	$C_D$	$C_L$
Mesh-1	0.250	0.928
Mesh-2	0.254	0.955
Mesh-3	0.255	0.953

### 3. Results and Discussion

#### 3.1 Experimental validation, error and uncertainty analysis

Experimental validation was conducted to benchmark the experimental procedure. The experimental data was validated with a NACA 0012 wing model with reference data at different Reynolds numbers in the wind tunnel. Across the entire investigation, the maximum standard error in the lift was 0.34, corresponding to a standard deviation of 0.67. For the drag, the maximum standard error was 0.09, corresponding to a standard deviation of 0.18. Therefore, repeatability was established in the experimental procedure, shown by Figure 8. The standard deviation and standard error of lift and drag data across experiments for specific  $\alpha$  values is outlined in (6) and (7), where ‘n’ is the number of values across experiments for a given  $\alpha$  in the sample, ‘ $x_i$ ’ is a data value, and ‘ $\bar{x}$ ’ is the mean of those data values.

$$SD = \frac{\Sigma(x_i - \bar{x})^2}{n} \tag{6}$$

$$SE = \frac{SD}{\sqrt{n}} \tag{7}$$

The uncertainty in the calculation of ambient density is a combination of the percentage uncertainties in the measurements of the ambient temperature and pressure of the wind tunnel and was determined to be 0.66%. to determine the uncertainty in  $V^2$  this was determined from the dynamic pressure and the height of the water column monometer that was attached to the wind tunnel pitot tube demonstrated in equation 2. The magnitude of the lift and drag force are function of the density, the wind tunnel square inlet velocity and the lift and drag coefficient.  $C_L$  and  $C_D$  are inherent properties of the wing models, and they are not measured. They are calculated from the lift and drag data after experimental analysis. Therefore, the ambient density and wind tunnel inlet velocity are the main drivers for uncertainty in the experimental investigation. Their percentage uncertainties add up. From error propagation principles, the uncertainty in the lift and drag data was determined to be approximately 5.2%.

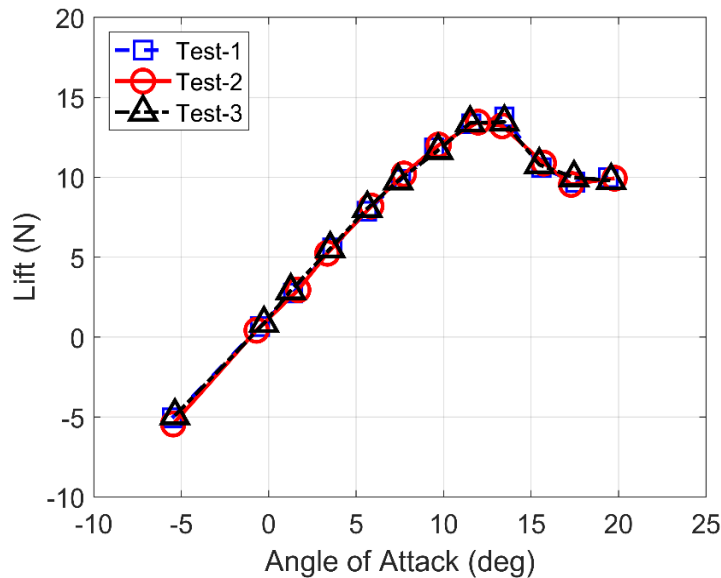


Fig. 8: Lift data obtained from NACA 0012 wing model during experimental validation.

### 3.2 Validation of the model

The lift and drag coefficient predicted by the numerical model at angle of attack varying from  $-5^\circ$  to  $25^\circ$  were compared with the in-house experimental results. The corresponding results are presented in Figure 9. It is evident from this figure that the numerical model is capturing the trend of experimental results for both lift and drag coefficient.

It can be observed figure 9(a) that the predicted lift coefficient is in close agreement with the experimental results. The predictions are within the experimental uncertainty range. A maximum deviation of 14% in lift coefficient is observed at  $AOA = 25^\circ$  from the experimental results. The numerical predictions of drag coefficient are in good agreement with the experimental results for  $-5^\circ \leq AOA \leq 15^\circ$  as can be seen in Figure 9(b). Moreover, at higher AOA ( $AOA > 15^\circ$ ), the deviation increases. A maximum deviation of 28% in drag coefficient is observed at  $AOA = 25^\circ$  from the experimental results. This is attributed to the limitations of two-equation RANS model in accurately resolving the post-stall flow regime.

Overall, the numerical predictions are comparable with the experimental results and hence can be used for comparative analysis.

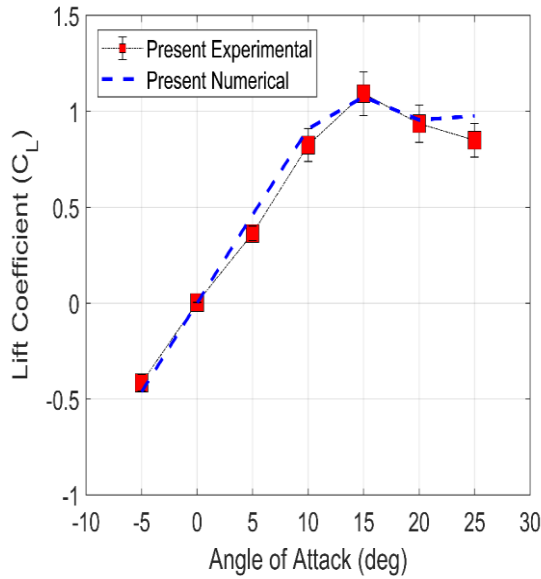


Fig. 9(a): Comparison of experimental and numerical results at various angle of attack - Lift Coefficient.

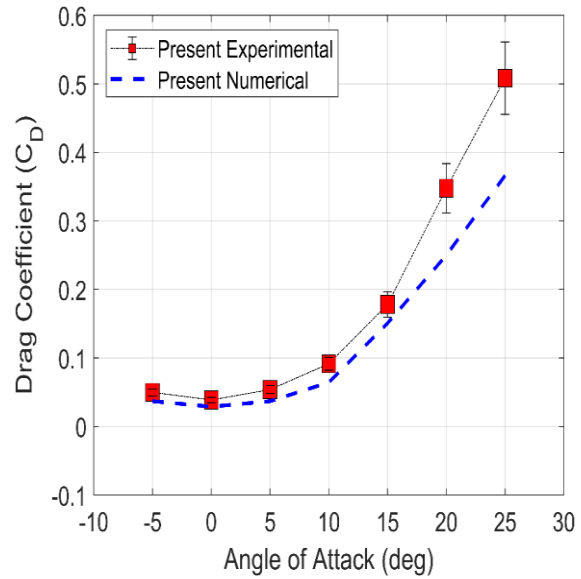


Fig. 9(b): Comparison of experimental and numerical results at various angle of attack - Drag Coefficient.

### 3.3 Influence of Amplitude of Leading-Edge Tubercle

Aerodynamic analysis was conducted on the designed wing models. Performance comparisons can be made from Figure 10

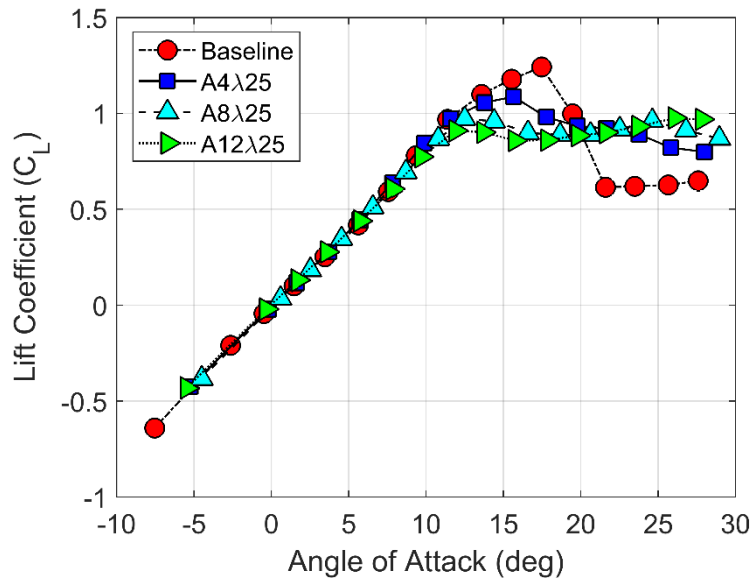


Fig. 10: Lift coefficient of the designed wing models.

The TLE aerofoils do not generate as much lift as the 'Baseline' wing, and they exhibit premature stall. All the wings have identical performance in lift generation up until a moderate  $\alpha \approx 10^\circ$ . The 'Baseline' wing's  $\alpha$  (Angle of Attack) stall =  $17.5^\circ$ , whilst  $\alpha$  stall =  $11.9^\circ$  for 'A12 $\lambda$ 25', which is a significant reduction. 'A4 $\lambda$ 25' and 'A8 $\lambda$ 25' stall within this range, with 'A4 $\lambda$ 25' being closely comparable to the 'Baseline'. Despite premature stall in the TLE aerofoils, a very gradual loss of lift is experienced. Thus, stall delay is attained. The improved post-stall performance concurs with observations from past research (Miklosovic, 2004). For the 'Baseline' aerofoil,  $C_{Lmax} = 1.24$ , whilst  $C_{Lmax} = 0.97$  for 'A12 $\lambda$ 25', representing a 21.8% reduction in lift generation capability from

incorporating large tubercles. As tubercle amplitude is increased, lift generation decreases. The decreasing  $C_{Lmax}$  from 'A4 $\lambda$ 25' to 'A12 $\lambda$ 25' highlights this. However, despite 'A12 $\lambda$ 25' having the lowest  $C_{Lmax}$ , it delivers the softest stall since it experiences negligible loss of lift and exhibits an upward trend in lift generation in deep post-stall flight. Since larger tubercles induce greater streamwise vorticity within the flow, greater lift generation is achieved in deep post-stall flight. These results comply with findings in Hansen's study, where the smallest tubercle amplitude model generated the greatest amount of lift (Hansen et al., 2011), and Rostamzadeh's observations of TLE wings with larger  $A/\lambda$  ratios exhibiting reduced pre-stall performance (Rostamzadeh, 2014).

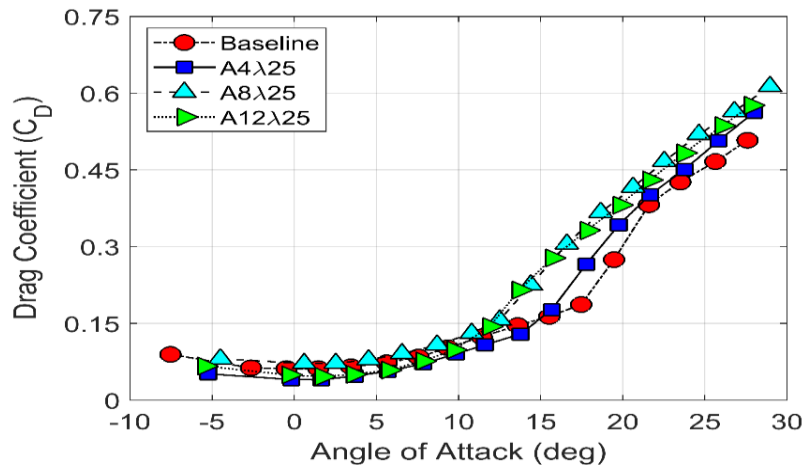


Fig. 11: Drag coefficient of the designed aerofoil models.

Figure 11 shows that the TLE aerofoils have a lower drag penalty (until stall). For the TLE wings,  $C_{Dmin}$  is 0.040, 0.071, and 0.046 for 'A4 $\lambda$ 25', 'A8 $\lambda$ 25', and 'A12 $\lambda$ 25', respectively, compared to the 'Baseline' aerofoil  $C_{Dmin}$  of 0.062. Therefore, the TLE aerofoils offer a lower drag penalty. The performance of 'A8 $\lambda$ 25' is anomalous, as it produces more drag than the 'Baseline' in both pre-stall and post-stall region. In post-stall region, 'A12 $\lambda$ 25' performs similarly to 'A8 $\lambda$ 25', producing equally high drag levels. Both aerofoils generate more drag in post-stall domain than the 'Baseline' aerofoil. 'A4 $\lambda$ 25' behaves similarly as it also produces increased drag in post-stall flight, yet it's not much greater than the 'Baseline'. Despite the TLE aerofoils posing increased post-stall drag, their reduced pre-stall drag, and improved post-stall lift generation capability offset this, resulting in enhanced aerodynamic efficiency, highlighted in Figure 12.

With observations from the  $C_L$  and  $C_D$  plots, combined with a plot of the aerodynamic efficiency, 'A4 $\lambda$ 25' is immediately realized as the better-performing TLE aerofoil. It provides the best aerodynamic efficiency for a large  $\alpha$  range. The 'Baseline' aerofoil only has improved aerodynamic efficiency in a small  $\alpha$  range of  $\sim 16^\circ - 19^\circ$ . 'A12 $\lambda$ 25' also depicts an improved aerodynamic efficiency compared to the 'Baseline' aerofoil in its pre-stall domain up until  $\alpha \approx 10^\circ$ , yet it's less efficient than 'A4 $\lambda$ 25' overall. The performance of 'A8 $\lambda$ 25' is skewed unfavorably due to its abnormally high drag values, which result in poorer aerodynamic efficiency. It's unlikely that the performance issues of 'A8 $\lambda$ 25' arose due to its geometry since it should offer intermediate performance. Surface defects are probable to cause poorer (than expected) performance characteristics.

### 3.3 Influence of angle of attack

The experimental measurements for Lift and Drag coefficients showed that the model with lesser amplitude in the TLE aerofoil was more efficient in creating lift and reducing drag. For this, model A4 $\lambda$ 25 has been numerically simulated and visualized to better understand the mechanism with respect to the varying angle of attack. The factors that were studied in detail for each angle of attack include a variation of Pressure coefficient ( $C_p$ ) at a different location on a tubercle location with respect to chord-wise length (i.e., Pressure Coefficient Vs. Chord at various  $Z/\lambda = 0, 0.25, 0.5, 0.75, 1.0$ ), surface streamlines, and x velocity at different chord lengths ( $x/c = -0.2, 0, 0.2, 0.6, 0.8$ ) for vortex visualization.

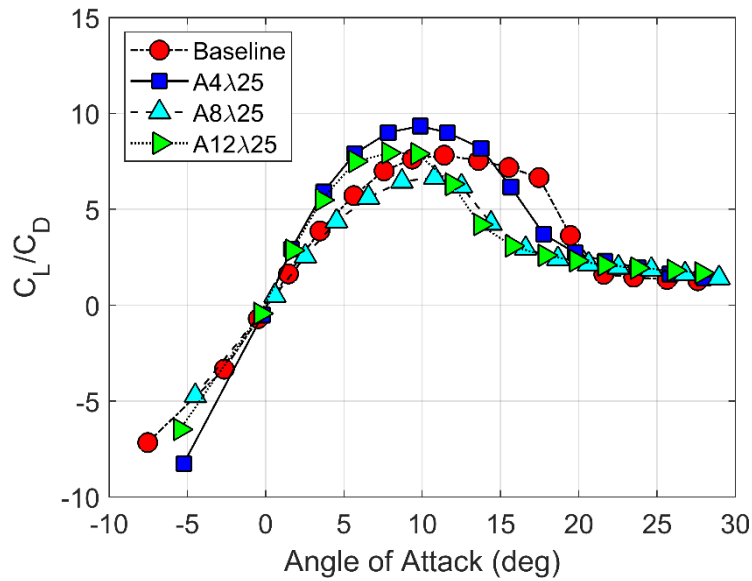


Fig. 12: Aerodynamic efficiency of the designed aerofoil models

### 3.4 Pressure coefficient variation

As seen in Figure 13(a), the model experiences the highest and lowest pressure coefficient values at the aerofoil's trough. These peaks of the Pressure coefficient gradually decrease as the Z value moves toward the crest. This trend is observed as the attack angle increases up to the stall angle. The peaks of the Pressure coefficient become steeper and move towards the leading edge of the aerofoil as the AOA is increased figure 13 (a-g). After the stall angle, the trend of the highest  $C_p$  peaks at the trough of the tubercle is interrupted. Figure 3(f) and figure 13(g) shows AOA 20° and AOA 25° having  $C_p$  peaks at the crest comparable to  $C_p$  peaks at the trough, and the peaks are unsymmetric with respect to the trough, signifying that  $C_p$  variation along the spanwise is also happening, thus indicating the presence of vortices that are dominant in the post-stall regime. The magnitude of  $C_p$  peaks increases up to the stall angle of attack of around 16° and decreases gradually, which complies with the lift coefficient characteristics observed in Figure 13

Figure 13(g) shows AOA 20° and AOA 25° having  $C_p$  peaks at the crest comparable to  $C_p$  peaks at the trough, and the peaks are unsymmetric with respect to the trough, signifying that  $C_p$  variation along the spanwise is also happening, thus indicating the presence of vortices that are dominant in the post-stall regime. The magnitude of  $C_p$  peaks increases up to the stall angle of attack of around 16° and decreases gradually, which complies with the lift coefficient characteristics observed in Figure 13

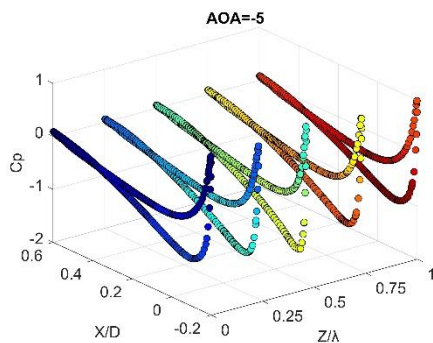


Fig. 13(a): Pressure coefficient vs. chord for varying  $Z/\lambda$  (with increasing AOA from a-g).

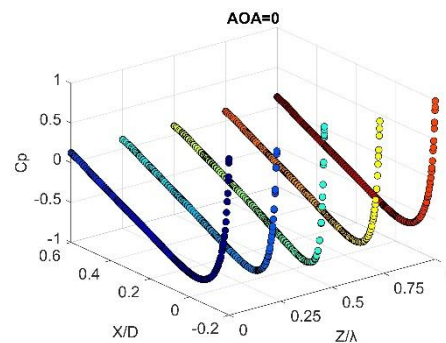


Fig. 13(b): Pressure coefficient vs. chord for varying  $Z/\lambda$  (with increasing AOA from a-g).

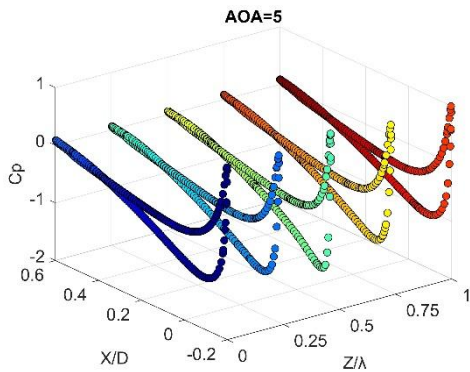


Fig. 13(c): Pressure coefficient vs. chord for varying  $Z/\lambda$  (with increasing AOA from a-g).

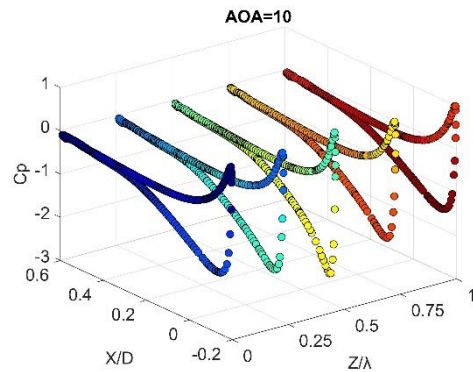


Fig. 13(d): Pressure coefficient vs. chord for varying  $Z/\lambda$  (with increasing AOA from a-g).

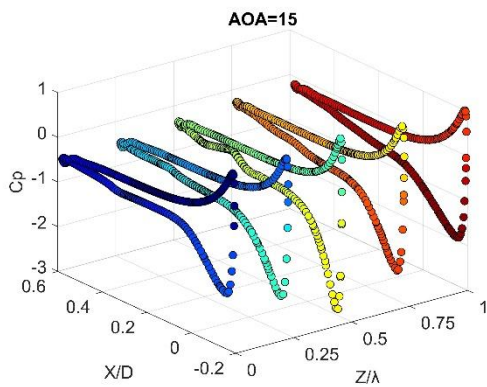


Fig. 13(e): Pressure coefficient vs. chord for varying  $Z/\lambda$  (with increasing AOA from a-g).

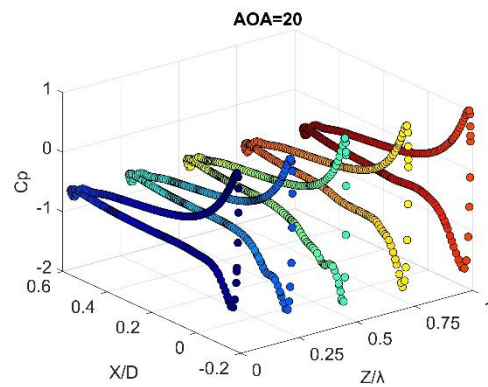


Fig. 13(f): Pressure coefficient vs. chord for varying  $Z/\lambda$  (with increasing AOA from a-g).

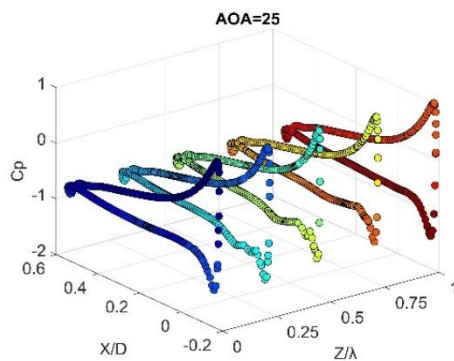


Fig. 13(g): Pressure coefficient vs. chord for varying  $Z/\lambda$  (with increasing AOA from a-g).

### 3.4.2 Surface streamlines visualization

The behaviour of airflow due to tubercles on different Pre-stall AOA can be understood through surface streamlines. The tendency of the flow to concentrate more towards troughs at the leading edge and then away from the troughs as it moves forward can be verified in Figure 14 to Figure 16. Figure 14 indicate lower velocity at the crests and higher velocity at the troughs. Furthermore, vortices of small magnitudes are created due to this concentration of air that had entered more in the trough moving away from the trough regions leading to patches/pockets of air near the trailing edge. A clear disruption zone at the chord end can be seen as the air moves forward. This disruption is the visualization of the vortices being created at the end of the wing. At AOA

0°, as the lift created is negligible, hence, the disruption or the vortices creation are of lesser magnitude, as seen in As the AOA of the wing increases, tubercles' effectiveness is enhanced. This is also accompanied by the oil patches of small air vortices in trough regions shifting more towards the leading edge. The effectiveness of the tubercles in vortex control can also be seen in the shapes of the patches created by vortices at the end of the aerofoil chord length. Instead of having a bigger patcher, the area of the patch is decreased by delaying the vortex formation in the trough regions. The higher velocity air from the trough leads to better suction of air at the upper surface, hence delaying stall.

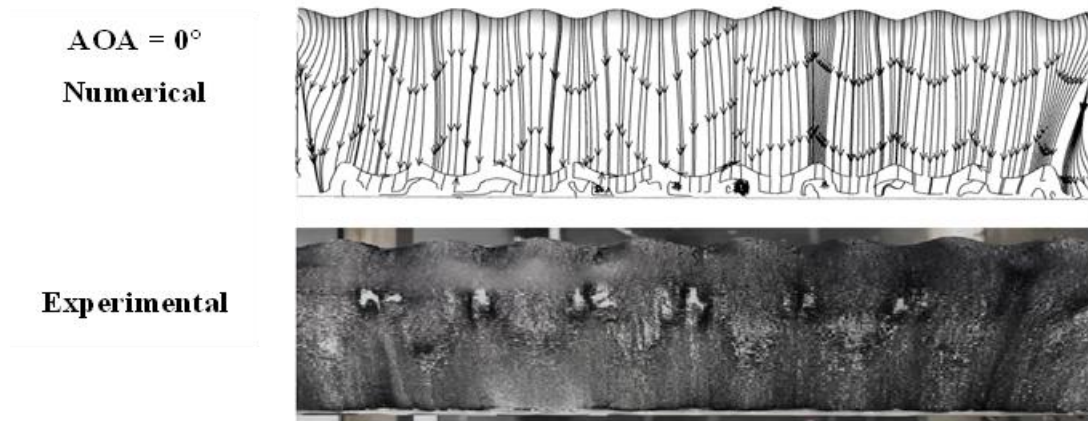


Fig. 14: Surface streamline visualization numerical and experimental for AOA 0°.

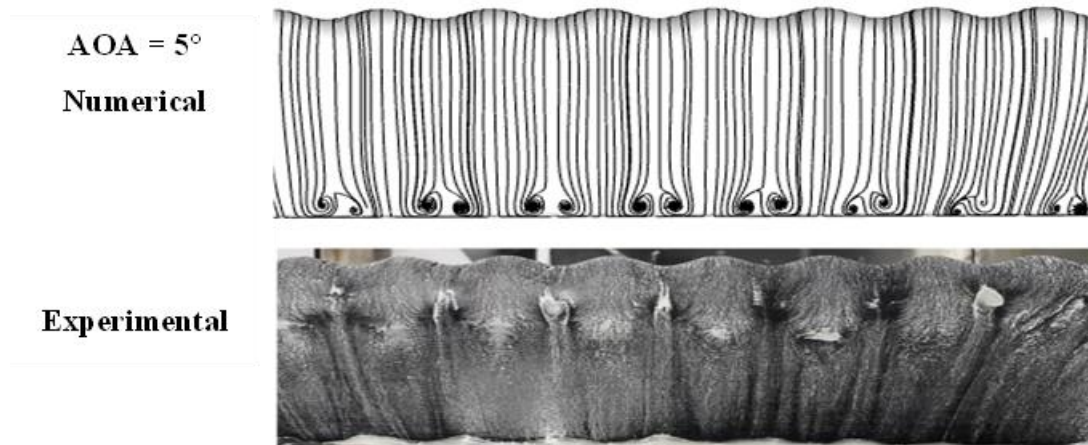


Fig. 15: Surface streamline visualization numerical and experimental for AOA 5°.



Fig. 16: Surface streamline visualization numerical and experimental for AOA 10°.

3.4.2 Path lines visualization

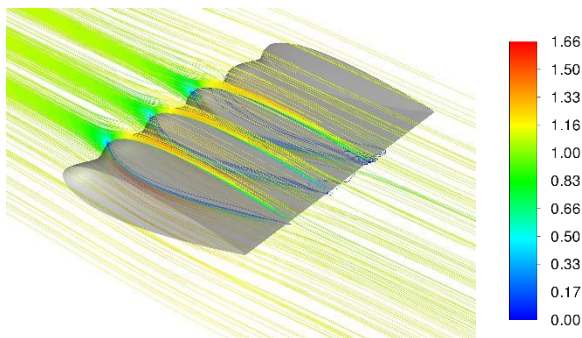


Fig. 17a: Streamline indicating flow pattern over TLE aerofoil for AOA =  $-5^\circ$

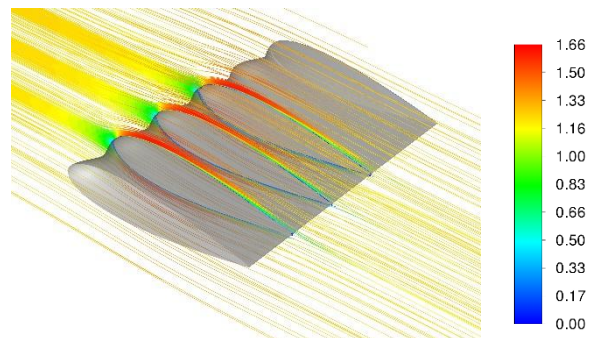


Fig. 17b: Streamline indicating flow pattern over TLE aerofoil for AOA =  $0^\circ$

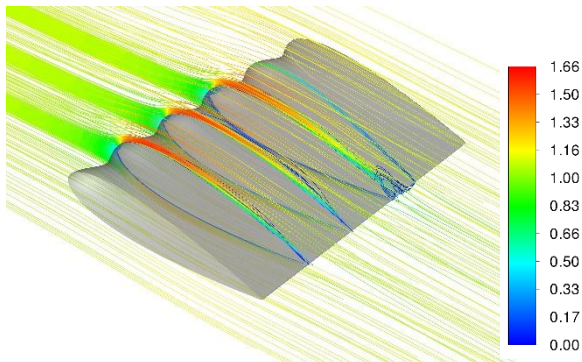


Fig. 17c: Streamline indicating flow pattern over TLE aerofoil for AOA =  $5^\circ$

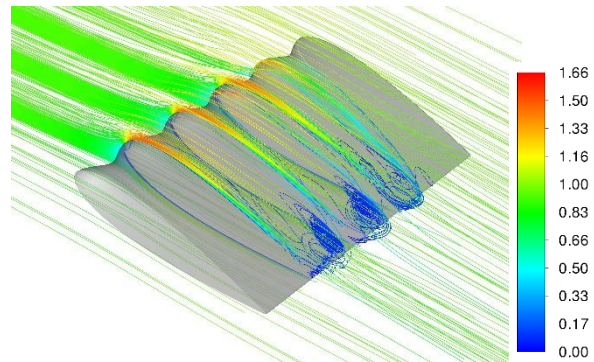


Fig. 17d: Streamline indicating flow pattern over TLE aerofoil for AOA =  $10^\circ$

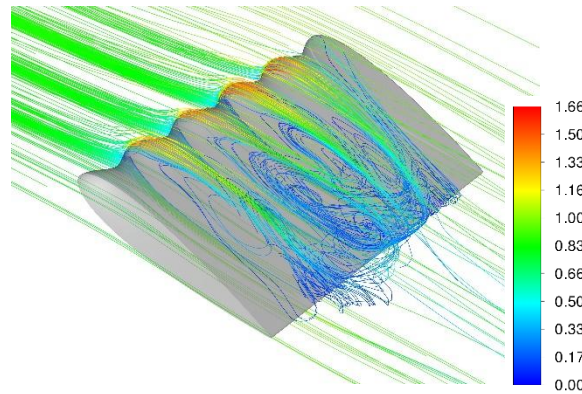


Fig. 17e: Streamline indicating flow pattern over TLE aerofoil for AOA =  $15^\circ$

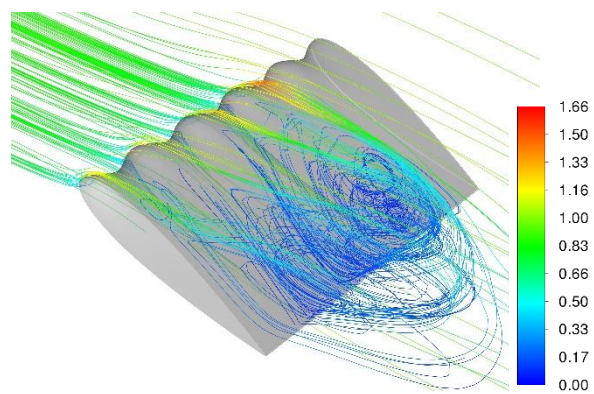


Fig. 17f: Streamline indicating flow pattern over TLE aerofoil for AOA =  $20^\circ$

Due to this difference in air velocity, the air from the trough region starts entering the region with lower velocity, creating pockets of vortices at the chord end of the trough region. Due to this vortex creation, the boundary layer separation is more controlled. As the angle of attack increases, especially after the stall, this higher velocity of flow in the trough separates from the surface earlier than the airflow flowing from the crest. This higher velocity air pushes the vortices creation more towards the leading edge, but the crest provides small regions near the leading edge where air does not separate from the surface as much, hence providing still some amount of lift. (the velocity scale is represented by  $U/U_{ms}$ ).

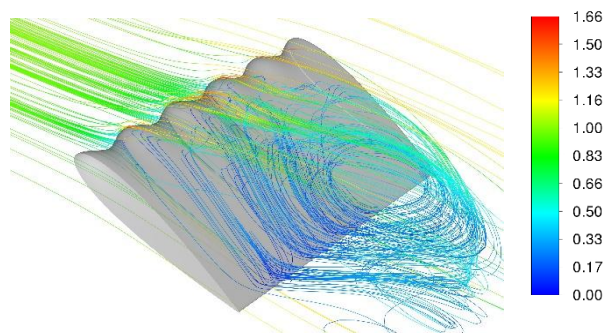


Fig. 17g: Streamline indicating flow pattern over TLE aerofoil for AOA = 25°

#### 4. Conclusion

TLE aerofoils are not commonplace, but small aerial vehicles requiring improved aerodynamic adaptability can benefit from their employment as well as marine fins and marine propulsors. The low Re performance of the designed TLE aerofoils exhibit similar performance enhancements observed at other Re values in past research (Hansen et al., 2011), (Gopinathan and Ralphin Rose, 2022) and they deliver mitigation against the increased stall severity. Therefore, there is considerable scope in implementing these TLE aerofoils in MAV and small UAV systems, in additions on marine propulsion and control systems since they operate under low Re regimes. From this study, the key observations of the designed TLE aerofoils include softer stall, delayed stall, a reduced drag penalty, and improved aerodynamic efficiency, with only a slightly decremented  $C_{Lmax}$ . Despite larger  $A/\lambda$  ratio TLE aerofoils generating increased vorticity and deep post-stall lift, 'A4 $\lambda$ 25' offers improved versatility. Its  $C_{Lmax} = 1.09$ ; only 12.1% lower than the 'Baseline'  $C_{Lmax}$  of 1.24. It exhibits the lowest  $C_D$  for a large  $\alpha$  range, resulting in superior aerodynamic efficiency. Despite weaker deep post-stall lift recovery in 'A4 $\lambda$ 25' compared to its larger TLE counterparts, it still provides the sought-after performance enhancements expected of TLE aerofoils. This study focused performance characteristics studies and visualizations to understand the mechanism of the model 'A4 $\lambda$ 25', which under experimental circumstances, is not viable.

The study indicates the trough region creates high-velocity air, which later gives rise to counter-rotating vortices that allow the re-energizing of the boundary layer at the end of the aerofoil chord length. This allows for the controlled creation of vortices to delay stall. Although this mechanism aids in stall delay, it does not aid in maximizing lift. Hence, demonstrating that these tubercles adaption on the leading-edge acts similar to stalling strip and not as vortex generators.

Eventually, the TLE aerofoils should be considered holistically in the context of an entire flight or marine system. Since efficiency and safety are paramount in these systems, comprehensive design and optimization is necessary. Consequently, a new generation of increasingly more popular and versatile small aerial vehicles and small marine unmanned vessels can be realized, in which severe stall and instability is a lesser issue. To achieve this, considerable work is necessary, but this biomimetic study shows the promising scope of this technology

#### Author Contributions:

H.L. performed the experimental work and the experimental analysis, and wrote part of the first draft of the paper. M.A.G. performed the computational work and CFD analysis. K.S. wrote and edited the CFD final draft of the paper. S.M.D. wrote and edited the final draft of the paper. M.A.G. was supervised by K.S., H.L. was supervised by S.M.D. Conceptualization by S.M.D.

**Funding:** The Research received no external funding

#### Acknowledgments:

The research was conducted in the frame work of H.L. towards of his MEng Degree in Aerospace Engineering at The University of Nottingham and in the frame work of M.A.G. internship at the University of Nottingham.

**Appendix:**

NACA 0012 tubercles profiles and dimensions are shown in Fig. A.1-3.

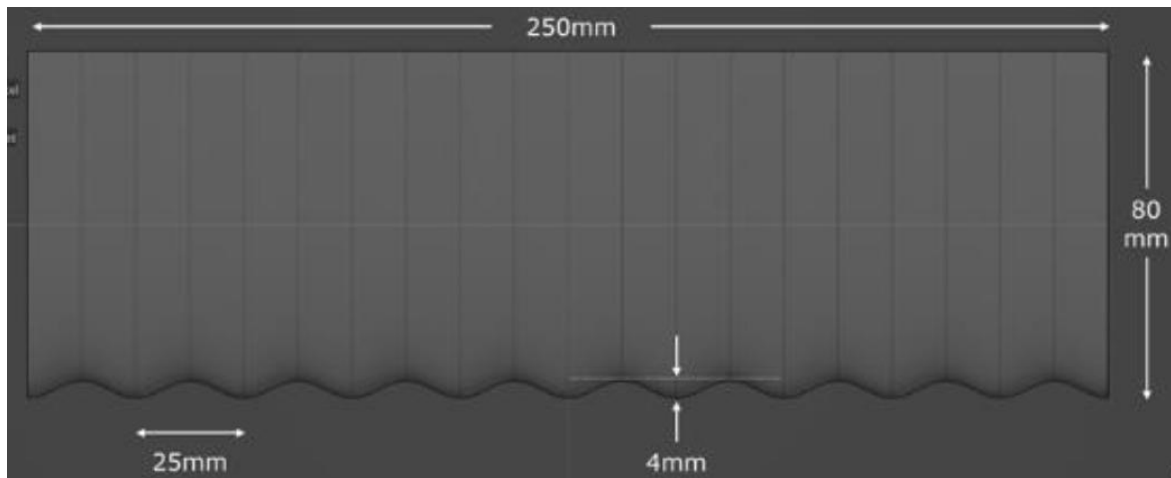


Fig. A.1: Amplitude 4mm, wavelength 25mm

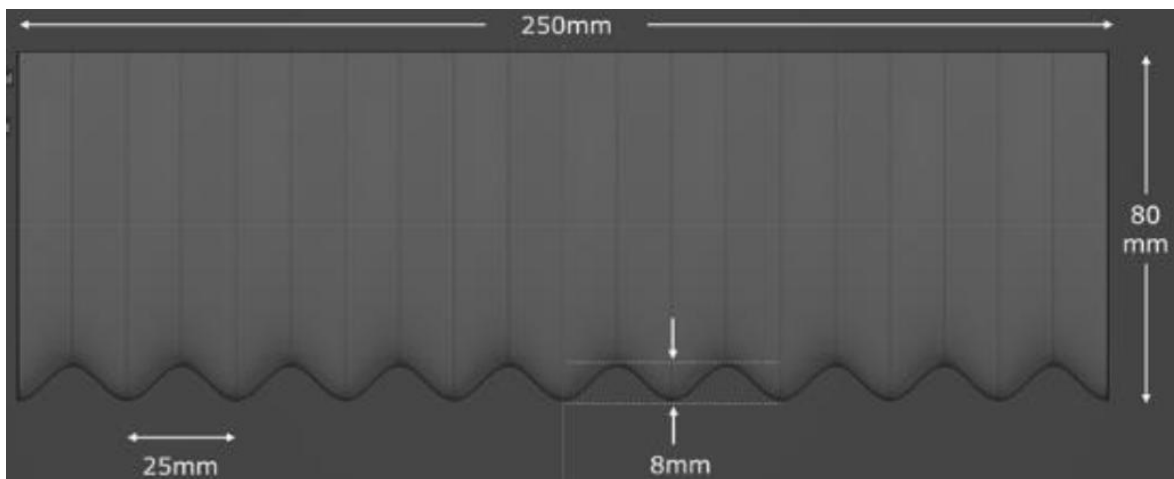


Fig. A.2: Amplitude 8mm, Wavelength 25mm

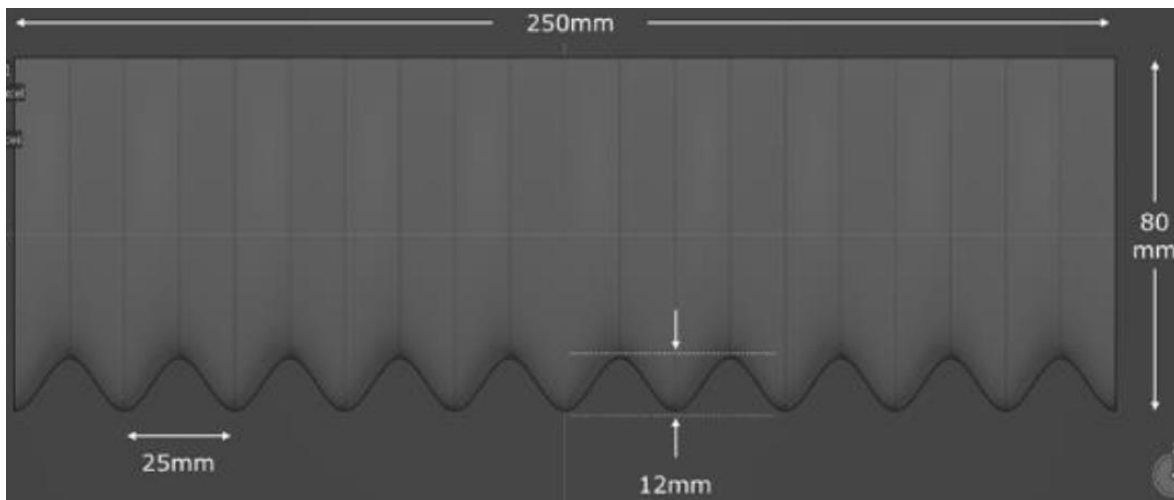


Fig. A.3: Amplitude 12mm, wavelength 25mm

## Camera specification and set-up

Oil flow visualization was conducted by capturing aerofoil flow surface pattern in-situ which was photographed by camera phone which was placed on top wind tunnel test section window in order to minimize reflection in captured photos. The device used was a Samsung Galaxy A5 (2017) SM-A520F model. Details of its camera can be found in the link: [https://m.gsmarena.com/samsung\\_galaxy\\_a5\\_\(2017\)-8494.php](https://m.gsmarena.com/samsung_galaxy_a5_(2017)-8494.php)

## Camera Specifications:

Single lens, 16MP, f/1.9 (F-stop), 27mm wide (35 mm focal length) AF (auto focus) with LED flash (on select images).

## Oil flow visualization procedure

1. A mixture of titanium dioxide (TiO<sub>2</sub>) powder, Paraffin and Linseed oil should be prepared. Titanium dioxide is suspended in Paraffin and placed in linseed oil container, in order to prevent clumping of the powder.
2. The optimal mixture starting point is 1g titanium dioxide powder, 1g of linseed oil and 10g paraffin oil.
3. The mixture should be thoroughly shaken in the sealed container and then transferring the content to the painting tray. The consistency of the mixture should be like a paint.
4. Apply the mixture to the model surface with a paint brush at the tested AOA while the wind tunnel is off. apply the mixture in a uniform manner along the spanwise direction
5. The paraffin will evaporate after around 10 seconds after turning the wind tunnel on, creating a dried surface flow pattern on the model surface. Due to this it vital to reach the wind tunnel velocity as quickly as possible.
6. Photograph the flow pattern in-situ after paraffin evaporated, this is conducted by placing a phone camera on the top of the wind tunnel test section window.
7. The paint residue can be wiped-off the surface of the model with a paper tissue.
8. Repeat steps 2 to 7 at AOA equal to 2, 5 and 10 degrees.

## References

- Aftab, S. M. A., Razak, N. A., Rafie, A. S. M., and Ahmad, K. A. (2016). Mimicking the humpback whale: An aerodynamic perspective. *Progress in Aerospace Sciences*, 84, 48–69. <https://doi.org/10.1016/j.paerosci.2016.03.002>
- Airbus. (2021). Biomimicry Imitating Nature's Best-Kept Secrets. Retrieved on 8 April 2024. <https://www.airbus.com/innovation/future-concepts/biomimicry.html#proj>.
- Airfoil tools (n.d.): Airfoil Tools. Retrieved 20 November 2021. <http://airfoiltools.com/index>
- ANSYS (2018): FLUENT User's Guide.
- Bal, S. (2024). Numerical investigation of 3-D wing moving over free surface in water of finite depth. *Journal of Naval Architecture and Marine Engineering*, 21(14). <http://dx.doi.org/10.3329/jname.v21i1.69871>
- Bandyopadhyay, P. R. (2009). Swimming and Flying in Nature—The Route toward Applications: The Freeman Scholar Lecture. *Journal of Fluids Engineering-transactions of the ASME*, 131(3). <https://doi.org/10.1115/1.3063687>
- Çelik, İ., and Li, J. (n.d.). Assessment of numerical uncertainty for the calculations of turbulent flow over a backward-facing step. *International Journal for Numerical Methods in Fluids*, 49(9), 1015–1031. <https://doi.org/10.1002/flid.1040>
- Dewar, S., Watts, P. and Fish, F. (2018). Turbines and fans inspired by whales, European Patent Office. Retrieved April 8, 2024 from <https://www.youtube.com/watch?v=55K9j4om4DU>
- Gopinathan, V. T., and Rose, J. (2022). Aerodynamic performance characterization of bio-inspired wings with leading edge tubercles at low Reynolds number. *Proceedings of the Institution of Mechanical Engineers. Part G, Journal of Aerospace Engineering*, 237(3), 561–586. <https://doi.org/10.1177/09544100221103737>
- Hansen, K. L. (2012). The effect of leading edge tubercles on airfoil performance, PhD Thesis. University of Adelaide.
- Hansen, K. L., Kelso, R., and Dally, B. B. (2011). Performance variations of leading-edge tubercles for distinct airfoil profiles. *AIAA Journal*, 49(1), 185–194. <https://doi.org/10.2514/1.j050631>
- Lositaño, I. C. M. and Danao, L. A. M. (2019). Steady wind performance of a 5 kW three-bladed H-rotor Darrieus Vertical axis wind turbine (VAWT) with cambered tubercle leading edge (TLE) blades. *Energy*, 175(C), 278–291. <https://doi.org/10.1016/j.energy.2019.03.033>

- Meredith, K. V. (Ed.). (2011). A numerical model for partially-wetted flow of thin liquid films (Vol. 70). <https://doi.org/10.2495/MPF110201>
- Miklosovic, D., Murray, M. M., Howle, L. E., and Fish, F. E. (2004). Leading-edge tubercles delay stall on humpback whale (*Megaptera novaeangliae*) flippers. *Physics of Fluids*, 16(5), L39–L42. <https://doi.org/10.1063/1.1688341>
- Patankar, S. V. (1980). *Numerical Heat Transfer and Fluid Flow*. CRC Press.
- Pattison, M. J. (2011). Secondary flows. *Thermopedia*. Retrieved April 8, 2024, from <https://www.thermopedia.com/content/1113/>
- Ray, S., Chatterjee, D., and Nandy, S. (2016). Unsteady CFD simulation of 3D AUV hull at different angles of attack. *Journal of Naval Architecture and Marine Engineering*, 13 111-123. <http://dx.doi.org/10.3329/jname.v13i2.25849>
- Rostamzadeh, N., Hansen, K. L., Kelso, R. M., and Dally, B. B. (2014). The formation mechanism and impact of streamwise vortices on NACA 0021 Airfoil's Performance with Undulating Leading Edge Modification. *Physics of Fluids* 26, 107101. <https://doi.org/10.1063/1.4896748>
- Rostamzadeh, N., Kelso, R., Dally, B. B., and Hansen, K. L. (2013). The effect of undulating leading-edge modifications on NACA 0021 airfoil characteristics. *Physics of Fluids*, 25(11). <https://doi.org/10.1063/1.4828703>
- Sakthivel., R., Vengadesan, S., and Bhattacharyya S.K. (2011). Application of non-linear  $\kappa$ - $\epsilon$  turbulence model in flow simulation over under water axisymmetric hull at higher angles of attack. *Journal of Naval Architecture and Marine Engineering* 2 149-163. <https://doi.org/10.3329/jname.v8i2.6984>
- Skillen, A., Revell, A., Pinelli, A., Piomelli, U., and Favier, J. (2014). Flow over a wing with leading-edge undulations. *AIAA Journal*, 53(2), 464–472. <https://doi.org/10.2514/1.j053142>
- TecQuipment Ltd (2010): AF100 Subsonic Wind Tunnel User Guide.
- Watts, P., and Fish, F. E. (2001). The influence of passive, leading edge tubercles on wing performance. <https://api.semanticscholar.org/CorpusID:201754345>
- WDC (2012) Humpback whale *Megaptera novaeangliae*. Retrieved 8 April 2024 from <https://uk.whales.org/whales-dolphins/species-guide/humpback-whale/>